

Article

Numerical Evaluation on Thermal Performance of 3D Printed Concrete Walls: The Effects of Lattice Type, Filament Width and Granular Filling Material

Kunda Chamatete ^{1,2} and Çağlar Yalçınkaya ^{2,*} 

¹ The Graduate School of Natural and Applied Sciences, Dokuz Eylül University, 35390 İzmir, Türkiye; kunda.chamatete@ogr.deu.edu.tr

² Department of Civil Engineering, Faculty of Engineering, Dokuz Eylül University, 35390 İzmir, Türkiye

* Correspondence: caglar.yalcinkaya@deu.edu.tr

Abstract: Three-dimensional concrete printing (3DCP) is of great interest to scientists and the construction industry to bring automation to structural engineering applications. However, studies on the thermal performance of three-dimensional printed concrete (3DPC) building envelopes are limited, despite their potential to provide a long-term solution to modern construction challenges. This work is a numerical study to examine the impact of infill geometry on 3DPC lattice envelope thermal performance. Three different lattice structures were modeled to have the same thickness and nearly equal contour lengths, voids, and insulation percentages. Additionally, the effects of filament width and the application of granular insulating materials (expanded polystyrene beads and loose-fill perlite) were also studied. Finally, the efficacy of insulation was established. Results show that void area affects the thermal performance of 3DPC envelopes under stagnant air conditions, while web length, filament width, and contact (intersection) area between the webs and face shells affect the thermal behavior when cavities are filled with insulating materials due to thermal bridging. The thermal efficiency of insulation, which shows the effective use of insulation, varies between 26 and 44%, due to thermal bridges.



Citation: Chamatete, K.; Yalçınkaya, Ç. Numerical Evaluation on Thermal Performance of 3D Printed Concrete Walls: The Effects of Lattice Type, Filament Width and Granular Filling Material. *Buildings* **2024**, *14*, 926. <https://doi.org/10.3390/buildings14040926>

Academic Editors: José Marcos Ortega and Fernando G. Branco

Received: 24 February 2024

Revised: 15 March 2024

Accepted: 24 March 2024

Published: 28 March 2024



Copyright: © 2024 by the authors. Licensee MDPI, Basel, Switzerland. This article is an open access article distributed under the terms and conditions of the Creative Commons Attribution (CC BY) license (<https://creativecommons.org/licenses/by/4.0/>).

Keywords: thermal performance; 3D printed concrete; energy-efficient buildings; thermal bridging; finite element modeling; insulation performance

1. Introduction

The construction industry consumes more than half of all raw materials globally, emits the most carbon, and accounts for 40% of total energy consumed globally [1]. This has a significant environmental impact because of its energy consumption. Three-dimensional printed concrete (3DPC) has emerged as a potential answer as the building sector changes to meet the demands of sustainability and environmental responsibility. This revolutionary technique is altering traditional construction practices by promising increased material and energy efficiency [2,3]. Three-dimensional concrete printing (3DCP) can reduce the environmental impact of material transportation by moving production directly to the construction site [4]. Furthermore, recent research into the incorporation of recycled elements implies that 3DCP can help reduce waste [5]. As a result, with increased knowledge of environmental protection legislation, the perception of sustainable growth in the construction industry is gaining traction. These days, the primary goal is to create a built environment that uses as little energy as possible [6].

Additive manufacturing presents a multitude of promising commercial prospects, with one of its key strengths lying in the capacity for product personalization [7]. Largely attributed to its rapid prototyping, customizable features, and just-in-time production capabilities, this technology has unlocked many profitable avenues across various industries [8].

Businesses are strategically leveraging the perks of 3D printing by leveraging diverse printing processes and approaches. Notably, two techniques, the Material Deposition Method (MDM) and binder jetting stand out as optimal for large-scale construction and small-scale architectural components, respectively [9].

The innovative MDM utilizes a nozzle to deposit construction material in a layered fashion, often as extruded concrete or mortar to construct 3D printed structures [9]. In their study, Mechtcherine et al. [10] investigated the application of MDM in construction, with a focus on creating building components using a robotic extrusion system. This cutting-edge technology has also been adopted by companies like Apis Cor, a pioneering construction startup, for on-site 3D printing of buildings. Their approach involves utilizing on-site robotic extrusion of construction materials to fabricate walls and structural elements [11].

Walls serve a crucial purpose in maintaining a stable internal microclimate within a building. Beyond just being resilient and long-lasting, these walls must also effectively block heat loss, excessive heat in the summer, noise pollution, and an increase in humidity. In response to the growing emphasis on energy sustainability in construction, 3DPC structures have emerged as a promising solution for achieving this objective [2,12]. A key factor to consider in the assessment of a building's heat transfer capabilities is its thermal transmittance, also known as the U-value. This value expresses the rate at which heat flows through a material or assembly. Accurate U-value predictions are crucial in assessing various building components such as walls, roofs, and windows. These metrics are instrumental in projecting a building's energy consumption and ensuring thermal comfort. However, determining U-values is no easy task, as the intricate process is influenced by multiple factors such as the materials used, junctions, and interfaces, all of which play a critical role in heat transfer. Sophisticated modeling methods, such as finite element (FE) analysis and computational fluid dynamics (CFD), offer more accurate predictions of U-values for intricate systems.

A variety of factors, including cavity size, geometry changes, and the addition of insulation in cavities can influence optimization of thermal performance in 3DPC walls. Researchers like Mansouri et al. [13] showed that subdividing large cavities into smaller ones can significantly reduce heat flux. Nemova et al. [14] experimentally studied the thermal performance of 3DPC-enclosing structures. They were able to develop an innovative energy-efficient ventilated 3DPC envelope with a low thermal conductivity coefficient following the climatic zone. Alkhalidi and Hatuqay [9] focused on designing energy-efficient and low-cost dwelling units by balancing cavities and 3D-printed material. Similarly, Suntharalingam et al. [15] demonstrated that complex geometries, such as double-rowed honeycomb or lattice structures, enhance insulation by trapping air.

The cavity-insulating material used in previous studies [9,15], expanded polylactic acid (E-PLA), a bio-based foam material, still has limited applications. While E-PLA has a niche market due to its green characteristics when compared to traditional materials, it still has a higher cost, lower thermal resistance (R-value), high sensitivity to moisture, relatively poor fire resistance, limited availability in some regions, and a lack of extensive long-term performance data [16–18]. Similarly, AlZahrani et al. [19] investigated the energy efficiency of infill structures while maintaining equal void-to-concrete ratios. They found that modifying the infill structure of 3DPC walls affects their thermal conductivity. However, their study lacks clear information on the geometric parameters of all the walls and the structural considerations made.

Due to the lack of technical design standards in the additive manufacturing of concrete walls, studies on the evaluation of thermal performance can easily overlook the structural aspects of these walls. In almost all the studies delving into the thermal performance optimization of 3DPC walls, the premises of the selection of infill structures are not clearly addressed. Therefore, this study aims to examine the impact of the infill geometry on the energy performance of large-scale, commercially applied 3DPC walls using infill structures of sufficient structural integrity. The selection of infill structures used in this study is supported by experimental literature and industrial trends. This work studies the effects of

void area, filament width, and insulation on the thermal performance of 3DPC envelopes for the same thickness, contour lengths, and void and insulation percentages. Because they are widely available, granular insulating materials, namely expanded polystyrene (EPS) beads and loose-fill perlite, are used in this study. The choice of these materials is also motivated by many other factors, such as ease and versatility of application, conformity to irregular shapes, recyclability, sustainability, and cost. Moreover, this study also aims to assert the extent to which thermal bridges affect the effective usage of granular insulating materials.

2. Methodology and Analysis

Three types of walls were chosen, and a thorough parametric analysis was carried out to investigate how the internal structure (infill structure) impacts energy performance. The study established the impact of void area effects, filament width, and insulation on the thermal behavior of these lattice envelopes. A detailed explanation of the parametric study can be found in Section 2.2. In selecting the three infill structures used in this study, a comprehensive approach was adopted to ensure that the lattice structures not only possess adequate structural integrity but also aligned with current industrial trends. The heat transfer analysis utilized Ansys Workbench for modeling. Appropriate numerical heat transfer models were created and verified using published data.

EPS beads and loose-fill perlite were applied for cavity insulation. Table 1 shows the thermal properties of the 3DPC and cavity-insulating materials [20–22]. Lastly, an assessment of the thermal efficiency of insulation is made to assert the extent to which thermal bridges can produce significant heat losses, resulting in ineffective usage of the insulation material. This research contributes to the development of energy-efficient and sustainable 3DPC building envelopes. The sections that follow contain detailed information on the research's methodology.

Table 1. Thermal properties of materials.

Material	Density (kg/m ³)	Thermal Conductivity (W/m.K)	Specific Heat (J/g.K)	Source
Concrete Block	2300	1.750	1.000	[23]
3DPC	1950	0.979	0.972	[22,24]
Air	Ideal gas	0.0242	1.00643	[15]
EPS	40	0.03	1.25	[20,25]
Perlite	400	0.045	0.837	[21,25]

2.1. Development of the Finite Element Model

2.1.1. Heat Transfer Analysis

In the realm of heat transfer across 3DPC walls, there is a delicate interplay between conduction, convection, and radiation. Notably, conduction plays a dominant role in this process, which can be attributed to the thermal behavior of the still air entrapped within the infill and the comparatively low temperatures at the external surfaces. The stagnant air acts as an insulator, impeding heat transfer via convective and radiative means. Because air movement is restricted, conduction becomes the primary mechanism for heat movement inside this region of the walls [19].

Due to the unconfined nature of the surroundings, convective and radiative processes are prominent heat exchange mechanisms between ambient air and the interior and external wall surfaces. This enables greater fluid mobility and radiant energy exchange. However, the insulative properties of air cavities often decrease as the cavity size increases. Tamimi et al. [26] found that heat transfer studies using still air are unreliable for cavities larger than 200 mm. Large cavities suffer from the development of convection currents, reducing their insulating efficacy. In contrast, smaller cavities, with still air forming a stagnant layer, function as effective insulators [27].

For one-dimensional heat transfer analysis through a building component consisting of homogeneous layers, EN ISO 6946 [28] provides a simplified calculation method to

determine thermal transmittance. In the simplified calculation method, the principle of thermal resistance is applied, and the thermal transmittance (U) is given by:

$$U = \frac{1}{R_T} \quad (1)$$

To determine the total thermal resistance through homogeneous layers, every material layer must be considered. The design thermal values of the layers can be provided as either design thermal conductivity or design thermal resistance. For a given thermal conductivity (λ), the thermal resistance (R) of a layer with a thickness (L) is obtained by:

$$R = \frac{L}{\lambda} \quad (2)$$

As a result, the total thermal resistance (R_T) of a plane-building component made up of thermally homogeneous layers perpendicular to the heat flow is computed using the following expression:

$$R_T = R_{\text{conv},i} + R_{\text{layer},1} + R_{\text{layer},2} + \dots + R_{\text{layer},n} + R_{\text{conv},e} \quad (3)$$

$R_{\text{conv},i}$ and $R_{\text{conv},e}$ are the convective resistances of the internal and external surfaces, respectively. The heat flow (Q) through an assembly of homogeneous layers is directly proportional to the thermal transmittance (U) and is given by:

$$Q = U\Delta T \quad (4)$$

The 3DPC walls are a homogeneous medium with constant thermal conductivity. Equation (5) describes three-dimensional heat conduction via a 3DPC envelope, which considers temperature variations in all three spatial directions: x , y , and z .

Since granular insulating materials are used for cavity insulation, these materials have interconnected voids between the individual grains, forming a tortuous but continuous air path through them. The heat transfer mechanisms within voids include solid and gas conduction, gas convection, and long-wave radiation [29]. EPS cell sizes, for instance, may typically be in the range of 50–350 μm , and the air convection component is negligible. The heat transfer through granular materials in this study is therefore determined using conductive contributions only, as radiation is also negligible due to low-temperature conditions [30,31].

$$\frac{\partial T}{\partial t} = \alpha \left(\frac{\partial^2 T}{\partial x^2} + \frac{\partial^2 T}{\partial y^2} + \frac{\partial^2 T}{\partial z^2} \right) \quad (5)$$

where:

- T is the temperature as a function of x , y , z , and time t .
- α is the thermal diffusivity of the material.

When examining the correlation between structural loading and the thermal performance of masonry walls, the primary focus often lies in subjecting these walls to extremely high temperatures, such as in the case of a fire. The intense heat causes the masonry to bend towards the source of the fire, leading to potential issues with vertical loading after extended exposure. This is because the elements within the masonry become unstable laterally due to the significant stresses caused by moments from lateral displacement [32–34]. However, the small temperature differences applied in this study are not significant enough to produce thermal strains and, under certain conditions, generate stresses within the 3DPC walls. Therefore, unloaded 3DPC wall configurations were investigated in this study through an uncoupled heat-transfer analysis (structural analysis is not integrated).

The isotropic material model present in Ansys was employed throughout this study. In this model, heat conduction is considered to be homogeneous throughout the lattice structures, and the thermal properties do not vary significantly with direction. This means

that the lattice structures' response to temperature changes is consistent across its entire volume. Within the lattice structures, it is assumed that all material properties, including specific heat capacity and thermal conductivity, are uniform in all directions [35]. The material properties are fed directly into the constitutive model.

In this heat transfer investigation, two parallel surfaces were identified as isothermal with varying temperatures. As a result, a perpendicular heat flow between these surfaces was established while disregarding any heat flux in the other direction since the other boundaries are considered insulated (adiabatic). The convective surface heat-transfer coefficients for the external and internal environments were set according to the provisions of EN ISO 6946: $25 \text{ W/m}^2\cdot\text{K}$ and $7.69 \text{ W/m}^2\cdot\text{K}$, respectively [28]. The exterior and interior sink temperatures were determined to be 302.5 K and 297.5 K , respectively. To achieve a design temperature difference of 5 K , the ambient temperature was maintained at a constant 295.15 K . Surface average weighted heat flux results were derived from simulations, and U-values were calculated by dividing the surface average weighted heat flux with the design temperature difference. The empty cavities were modeled as air layers. The thermal conductivity of still air was determined by dividing the thickness of the air layer with unventilated air layer thermal transmittance values interpolated from the relevant table given in EN ISO 6946 [28]. Figure 1 shows the application of boundary conditions to the FE models.

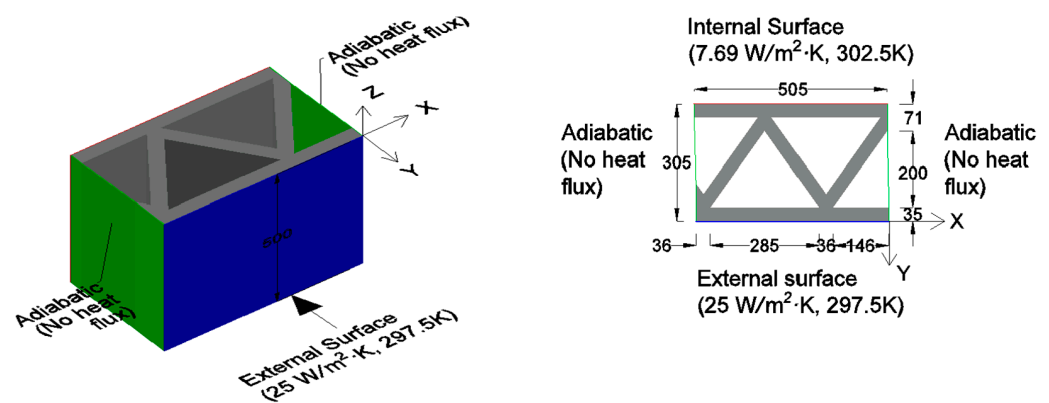


Figure 1. The application of boundary conditions to the FE models (dimensions in mm).

2.1.2. Mesh Sensitivity Analysis

Mesh sensitivity analysis was performed to find the ideal element size that produces the more accurate results while consuming the least amount of computational time and resources. To do so, seven various mesh size combinations of global and edge seedings were investigated in five cavity layouts of hollow concrete bricks selected from the work of Henrique dos Santos et al. [23]. They thermally characterized several cavity layouts of hollow concrete bricks. The cavity layouts selected for sensitivity analysis were B1, B3, B5, B7, and B9, and are provided in Figure 2. Edge seeding was used to selectively refine the mesh along edges or boundaries where higher mesh resolution is needed to improve the overall mesh quality. This sensitivity analysis's global/edge seeding combinations ranged from a very coarse combination of $20/2 \text{ mm}$ to a finer $3/2 \text{ mm}$. Figure 3 depicts the mesh sensitivity analysis.

Overall, the U-values decreased as the mesh sizes decreased. When the mesh combinations had global seedings greater than 8 mm , the decrease was significant; when the global seedings were less than 8 mm , the decrease was very minor and almost insignificant. In contrast, as the mesh sizes were reduced, the computing time increased. At $8/2 \text{ mm}$, there was a satisfactory balance between computational time and accuracy. The increase in computational time was large for $3/2 \text{ mm}$ as the lowest mesh size studied. Therefore, the $5/2 \text{ mm}$ combination was chosen to balance computing efficiency and accuracy, as well as to obtain clearer heat flux contour maps.

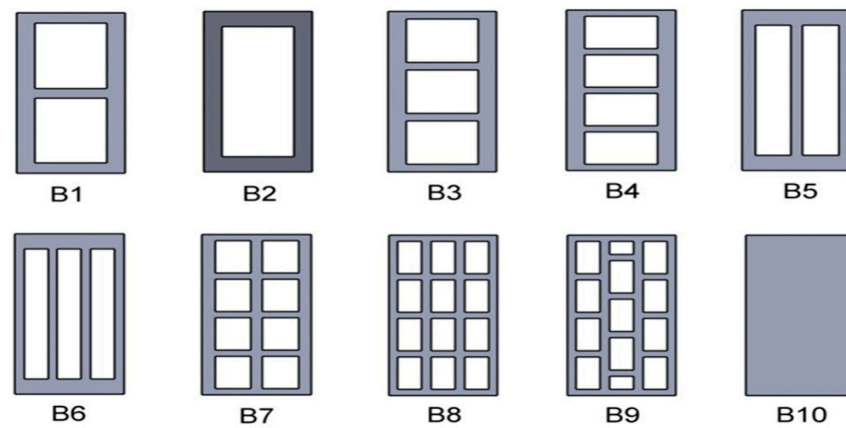


Figure 2. Hollow concrete block layouts studied [23]. Source: Henrique dos Santos, G., Fogiatto, M. A., and Mendes, N, numerical analysis of thermal transmittance of hollow concrete blocks. *Journal of Building Physics*, 41(1), 7–24, copyright © 2017 by SAGE Journals. Reprinted by Permission of SAGE Publications.

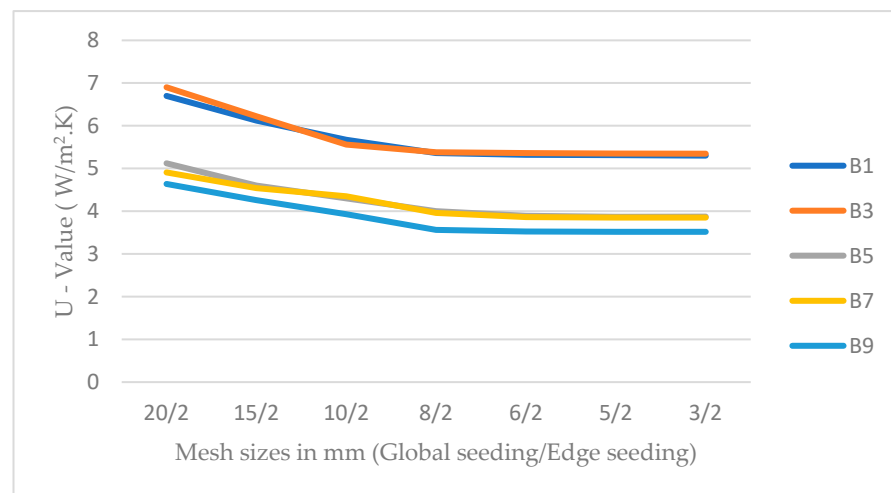


Figure 3. Mesh sensitivity analysis.

2.1.3. Validation of Finite Element Model

Validating finite element models is critical since it provides accuracy assessment, model implementation verification, and confidence building in the model's predictive capabilities. As a result, the simulation models developed were tested against previously published literature. The validation was performed against the work of Henrique dos Santos et al. [23]. They performed the thermal characterization of several cavity layouts of hollow concrete bricks. This was completed by comparing the thermal transmittances obtained from FE simulations to those calculated using the analytical methodology presented in international regulation (EN ISO 6946). Therefore, 10 cavity layouts of hollow concrete blocks, provided in Figure 2, were modeled and validated.

Figure 4 shows the U-value results obtained from the FE models developed by the authors and those calculated by Henrique dos Santos et al. for each block using EN ISO 6946. The simulation results are in good agreement with the standard values. The absolute average error is 2.88%, which is less than Henrique dos Santos et al.'s absolute average error of 3.81% when compared with their FEM (finite element modeling) results. Hence, the models are accurate and reliable and could be used for detailed parametric analysis of the energy performance of 3DPC building envelopes.

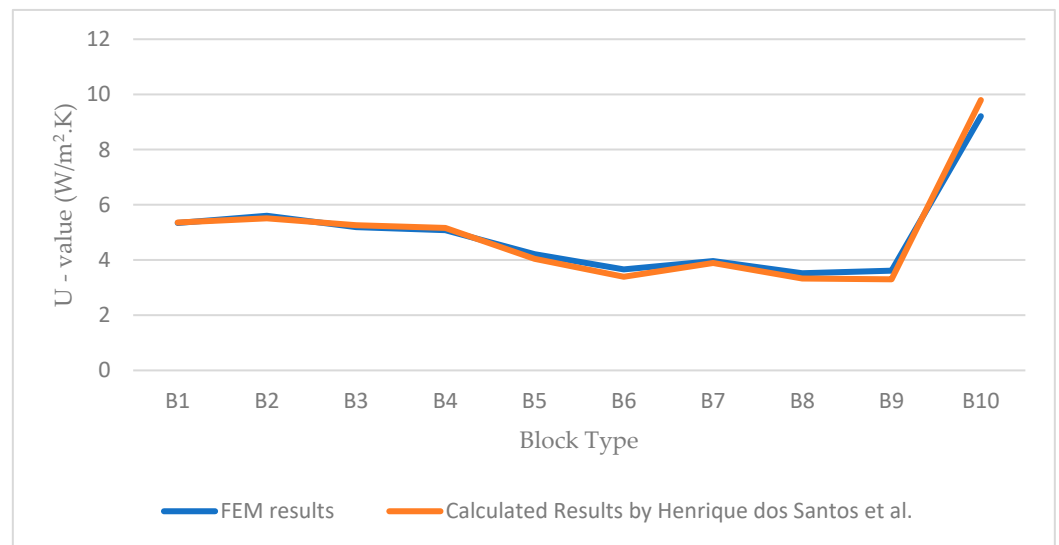


Figure 4. U-value results were obtained from the FE models developed by the author and those determined by Henrique dos Santos et al. [23].

The constitutive model used was also validated against the work of Tamimi et al. [26]. They studied the thermal performance of 3DPC walls both experimentally and numerically. They established the thermal transmittance values of the printed structures using heat flux meters and thermocouples. Figure 5 shows the wall geometry of Structure 1 adopted for validation.

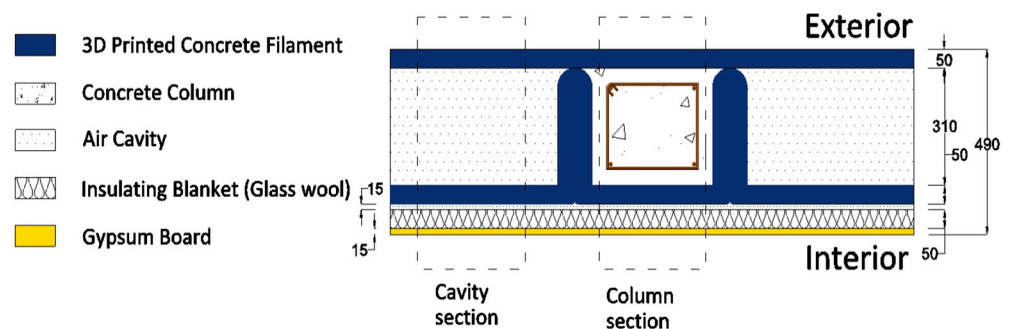


Figure 5. Plan view of Structure 1 (dimensions in mm). Source: redrawn based on data from Tamimi et al. [26].

For the in situ measurement of the U-value, tests were conducted for both the column and cavity locations of Structure 1. Therefore, two models were developed, and the U-values were determined with the application of the same boundary conditions. The thermal conductivities of 3DPC filament, concrete, gypsum board, glass wool, and steel are 0.781, 0.8, 0.159, 0.031, and 60.5 W/m.K, respectively [26].

The U-values from the FE simulations were 0.455 W/m².K and 0.410 W/m².K for the cavity and column locations, while those from in situ measurements were 0.440 W/m².K and 0.395 W/m².K, respectively [26]. Despite the respective errors of 3.41% and 3.80% in the simulated results, the results show very good agreement. These errors may be attributed to the nature of the construction of this 3DPC technology. Sun et al. [36] conducted an experimental study on the thermal performance of a 3DPC prototype building. They discovered that some 3D printing characteristics, such as the number of layers per printing, rest time during the printing process, and layer-by-layer appearance, can have adverse effects on 3DPC thermal performance and generate thermal defects. However, simplifications were made in the FE models such as assuming the wall panels to be straight-faced instead of the actual layer-by-layer appearance. Moreover, air may be entrapped between layers during

the printing process, creating voids that may be insulative. All these phenomena have the potential to affect the overall thermal performance of 3DPC envelopes. It may be expected for FE models to have a slightly higher U-values.

Assumptions on the size and spacing of the rebar were also made in the case of the column section due to a lack of clear information in the literature. For the longitudinal bars and lateral ties, 12 mm and 8 mm diameter bars at spacings of 50 mm (from faces of 3DPC) and 300 mm (center-to-center) were applied, respectively. Despite being minor by volume fraction of the concrete column, all these discrepancies may potentially affect the thermal resistance of the section. Therefore, the results of this validation can be relied on, as the errors are minimal and justifiable. The validation results also align with similar studies on heat conduction, such as Lu et al. [37]'s study. They conducted numerical modeling and experimental verification for the anisotropic heat conduction process in the velocity probe of the thermal mass flowmeter. Their results showed that the average relative error between the simulated results and experimental data was 2.92%, and the maximum relative error was 10.91%.

2.2. Parametric Study

A holistic selection approach was taken in the selection of the three infill structures used for the parametric study. This is to ensure that the lattice structures studied not only have sufficient structural integrity obtained from experimentation literature but are also consistent with additive manufacturing industrial trends. Despite several novel structures for in-fill materials proposed in the literature, the selection of the lattice structures was limited to three. This is because of the limited structural performance data, especially under axial compression, which is the main loading direction for wall systems. Most of the literature on the mechanical performance properties of 3DPC infill structures focuses on their flexural performance as beams, with loadings in the vertical (layer deposition direction) and transverse (layer translation direction) loading directions. Moreover, some of the proposed infill structures still do not have commercial applications among companies in the 3DPC business.

The first lattice structure (T) is a truss topology (zigzag) obtained from the work of Daungwilailuk et al. [38]. They experimentally studied the large-scale 3DPC walls under unconfined axial compression to determine the effect of different infill patterns on mechanical behavior. Their study indicated that the inner truss inside 3DPC plays a role in the wall bracing. It can mitigate the wall bowing and prevent the buckling failure of the wall. Joh et al. [39] note that when the wall and lateral supports are connected in parallel, there is a tendency for higher resistance to buckling. Companies like Black Buffalo and QOROX commonly use this wall type [40].

The second wall type (A) used in this study is a square zig-zag configuration obtained from Apis Cor, a Guinness Book World Record holder for the world's largest 3D-printed building on Earth. The company affirms that its 12" lattice structure is of the same structural integrity as a 12" concrete block wall [11].

Lastly, the third wall structure (P) is an innovative cob design adopted from the literature of Bello and Memari [40], who conducted an extensive review of the current state of 3D printing in the concrete industry. They looked at several companies currently in the additive manufacturing space and their approaches to the creation of 3DPC walls, including wall design. This cob design (the inside cavity is separated by a weave-like pattern) is unique to WASP, another leading company in the 3DPC industry based in Italy. In this wall design, no steel reinforcement is added to the wall, as the shape of the wall itself is designed to provide all the necessary strength [41,42]. Figure 6 shows the three wall types considered in the parametric analysis. The first, second, and third wall types are denoted by T, A, and P, respectively.

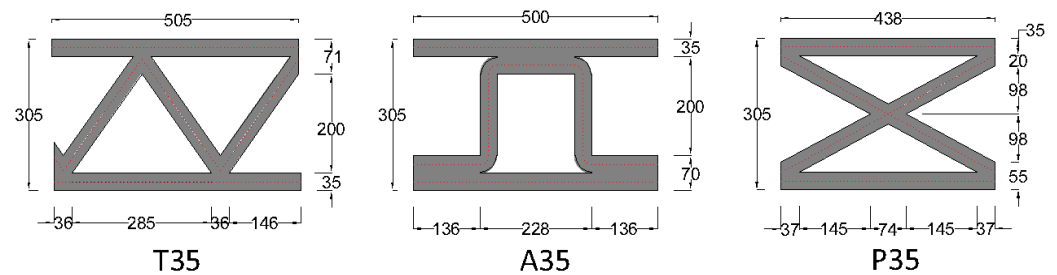


Figure 6. Wall types (35 mm filament width) for the parametric analysis (dimensions in mm).

To study the effects of void area, filament width, and insulation on the thermal performance of 3DPC envelopes, all the lattice structures under this study were modeled to have the same thickness, height, nearly equal contour lengths and void, and insulation percentages. All contour lengths were measured along the center lines of the respective filaments as shown by red-dotted lines in Figure 6. By keeping the void area constant, the concrete area was increased by varying the filament width. This was completed using three nozzle sizes, i.e., 35 mm, 40 mm, and 50 mm, established from common industrial practice (Table 2). In the large-scale 3D printing of buildings, many companies, like Black Buffalo 3D, the first company to receive a building code compliance, at material, machine, and structural wall levels, use nozzle sizes of 1.38''–1.97'' (35–50 mm) [43]. For the 35 and 40 mm nozzles, the contour lengths, void, and insulation percentages are almost identical, while minor differences can be seen with the 50 mm nozzle size. Additionally, the T and A walls have very close void areas, while the P walls have a slightly lower void area. All walls are modeled to have an initial thickness of 12 in. (304.8 mm) but increased slightly due to an increase in filament width. Furthermore, a constant wall height of 500 mm is maintained in all cases. A detailed description of the parametric study is given in Table 2, where T35 means wall type one with a 35 mm nozzle size. The same analogy applies to naming all the subsequent walls.

Table 2. Detailed description of the parametric study.

Wall	Nozzle Size (mm)	Contour Path Length (mm)	Concrete Area (mm ²)	Void Area (mm ²)	Void Percentage	Cavity Fill Material	No. of Models
T35	35	1870	63,872.03	89,680.7	58.4	Air, EPS and Perlite	3
T40	40	1897.66	73,951.28	89,680.7	54.8	Air, EPS and Perlite	3
T50	50	2038	89,682	89,680.7	50.0	Air, EPS and Perlite	3
A35	35	1869.6	65,434.4	86,965.55	57.1	Air, EPS and Perlite	3
A40	40	1882.98	74,771.5	86,965.55	53.8	Air, EPS and Perlite	3
A50	50	1919.38	94,047.2	86,965.55	48.0	Air, EPS and Perlite	3
P35	35	1870	62,505.79	70,996.6	53.2	Air, EPS and Perlite	3
P40	40	1915.1	90,217.24	70,996.6	44.0	Air, EPS and Perlite	3
P50	50	2005.5	94,269.93	70,996.6	43.0	Air, EPS and Perlite	3
Total							27

The thermal performance of building envelopes is significantly impacted by the design of their insulation. This design is heavily influenced by a financial trade-off between the initial investment in improving the envelope and the long-term cost of energy for maintaining the space, taking into account factors such as durability and maintenance expenses [44]. An important aspect of this study is the incorporation of granular insulating materials, i.e., loose-fill EPS beads and perlite, for cavity filling of the hollow 3DPC building envelopes. The choice of these materials is not only motivated by the demands of sustainability and environmental responsibility in the construction industry but also by the ease and versatility of application, conformity to irregular shapes, and cost-effectiveness offered by these materials. EPS insulation is a highly efficient and environmentally friendly option, known for its lightweight and sturdy composition. As stated by the Insulation Company of

America, it has always been free of harmful substances such as CFCs and HCFCs [45]. Its impressive characteristics, including its low thermal conductivity and lightweight structure, significantly reduce heat transfer in 3DPC structures [45,46]. Similarly, perlite, a naturally occurring inorganic mineral, is a long-lasting insulation material that can support its weight without settling or bridging. It boasts excellent thermal properties due to its amorphous volcanic glass structure and offers added protection against fires at a reasonable cost. Not only is perlite lightweight and easily poured, but it also does not require any special equipment or skills. This versatile material is mined and processed with minimal impact on the environment, making it a preferred choice for green communities who recognize its high-performance qualities [47,48].

Granular insulating materials, as stated earlier, have interconnected voids between the individual grains, forming a tortuous but continuous air path through them. Tests conducted by Simpson et al. [31] indicated that the thermal conductivity of loose EPS beads can be up to 5% higher than that of EPS boards of a similar density. Therefore, the thermal conductivity of the granular materials in this study was increased by 5%. A total of 27 wall models, with and without cavity insulation, are considered in the parametric study (Table 2). It is worth noting that in real-life construction, in all the wall systems, a portion of the wall cavities are filled with concrete and rebar, while others are reserved for services such as electrical and plumbing. To maintain consistency, the analysis was conducted without the presence of concrete and reinforcement, as well as service lines in the cavities.

2.3. Thermal Insulation of Efficiency

Although insulation materials are mostly cheaper than concrete materials, they considerably increase the overall cost of construction. Thus, the effective use of these materials for insulation is important. By studying the relative thermal efficiency (T_{Eff}) of insulation materials, the effectiveness of these materials in preventing the flow of thermal energy in building assemblies can be quantified and cost-optimized. Thermal insulation efficiency is used as a measure of the extent to which unintended thermal bridges can produce significant heat losses, resulting in ineffective usage of the insulation material. It is often quantified in terms of the R-value (thermal resistance) [49]. The higher the thermal resistance, the more efficient the insulation is at increasing the thermal inertia. Since thermal resistance and U-value are reciprocals, the higher the U-value, the less efficient the insulation is.

The method of estimating the T_{Eff} value in this study is based on an R-value comparison of insulated (R_{in}) and uninsulated (R_{un}) envelopes, each having the same face area (A_{fa}). The equivalent R-value (R_{eq}) of the insulation material alone is the R-value of insulation inserts into the cavities collectively per wall. It is calculated as an equivalent transformed layer of the total insulation material used for cavity filling, having the same face surface area (A_{fa}) as the wall under consideration and containing the same volume of insulation (V_{Tins}). The equivalent thickness of the insulation layer is the quotient of the total volume of insulation (V_{Tins}) divided by the face surface area (A_{fa}), while R_{eq} is the product of the equivalent thickness and the thermal resistivity of the insulation material [50]. T_{Eff} may be expressed by the following equation:

$$T_{Eff} = \frac{R_{in} - R_{un}}{R_{eq}} \times 100 \quad (6)$$

where

- R_{in} is the R-value of the insulated wall panel,
- R_{un} is the R-value of the uninsulated wall panel, and
- R_{eq} is the equivalent resistance of insulation material alone, configured as a single uninterrupted layer.

3. Results and Discussion

This section discusses the numerical simulation results of the parametric study. The thermal transmittance values of all the models are given in Table 3. For nearly the same contour lengths, the effects of infill shapes, voids, and insulation areas, as well as filament width, are discussed herein.

Table 3. Thermal transmittance values of all models in the parametric study.

Wall Configuration	U-Values (W/m ² .K)			Percentage Reduction (PR) (%)		Difference in PR (%)
	Air	Perlite	EPS	Perlite	EPS	
T35	3.485	0.509	0.445	85.39	87.23	1.84
T40	3.312	0.525	0.464	84.15	85.99	1.84
T50	3.093	0.593	0.534	80.83	82.74	1.91
A35	3.472	0.519	0.453	85.05	86.95	1.90
A40	3.296	0.559	0.496	83.04	84.95	1.91
A50	2.993	0.622	0.563	79.22	81.19	1.97
P35	2.77	0.489	0.417	82.35	84.95	2.60
P40	2.702	0.516	0.444	80.90	83.57	2.66
P50	2.459	0.558	0.49	77.31	80.07	2.77

3.1. Effect of Area of Stagnant Air

Overall, the U-values for T (truss-type) and A (zigzag-type) are very close, while those of P (weave-like pattern) are comparatively lower for nearly equal contour lengths (Table 3). In both the T and A walls, the thermal conductivities of the voids are the same due to identical air layer thicknesses (200 mm) (Figure 6). However, T walls have a slightly higher void area than A walls. T walls have a void area of 89,680.7 mm² while that of A walls is 86,965.55 mm² (Table 2). The difference in void area between the two wall types is 2715.15 mm². Despite the small difference, the void percentages in both wall types are almost identical for the same filament width. For instance, for the same 35 mm nozzle, the void percentages for the T35 and A35 walls are 58.4% and 57.06%, respectively. The voids of the P walls, on the other hand, have two types of air layers based on the different thicknesses of the air layers. The larger voids are of the same thickness as those of the T and A walls, while the smaller ones have almost half the thickness (98 mm) (Figure 6). Additionally, the P walls have the lowest void area, 70,996.6 mm², comparatively (Table 2). The void area differences between P and A walls and P walls are 18,684.1 mm² and 15,968.95 mm², respectively. Consequently, the void percentages of the P walls are lower for the same filament width.

Figure 7 shows the heat flow paths in the surface heat flux contour maps of the walls. In T and A walls, heat transfer occurs predominately through voids via gas conduction (vibration and collision of gas particles). This is because the total thermal conduction of the stagnant air volume considered is slightly higher than that of the 3DPC in both wall types. It should be noted that the thermal conductivity of stagnant air is proportional to the thickness of the air layer [28]. Thus, gas conduction is high in thick air layers. T35 has the highest U-value, 3.486 W/m².K, of all walls, indicating the poorest thermal performance (Table 3). P50 shows the best thermal performance under stagnant air conditions, with a U-value of 1.947 W/m².K. Furthermore, it is observed that for T and A walls of the same filament width (nozzle size), the U-values of the T walls are slightly higher than those of the A walls. For example, T40 has a U-value of 3.312 W/m².K while that of A40 is 3.296 W/m².K. The thermal behavior may be because of the difference in void areas. Additionally, a notable decrease in the U-values is seen across all wall types with an increase in filament width (nozzle size). This may be because of the increase in concrete areas and subsequent decrease in void percentage. Since most of the heat transfer occurs via the more conductive voids, an increase in filament width more or less acts as an insulative reverse effect.

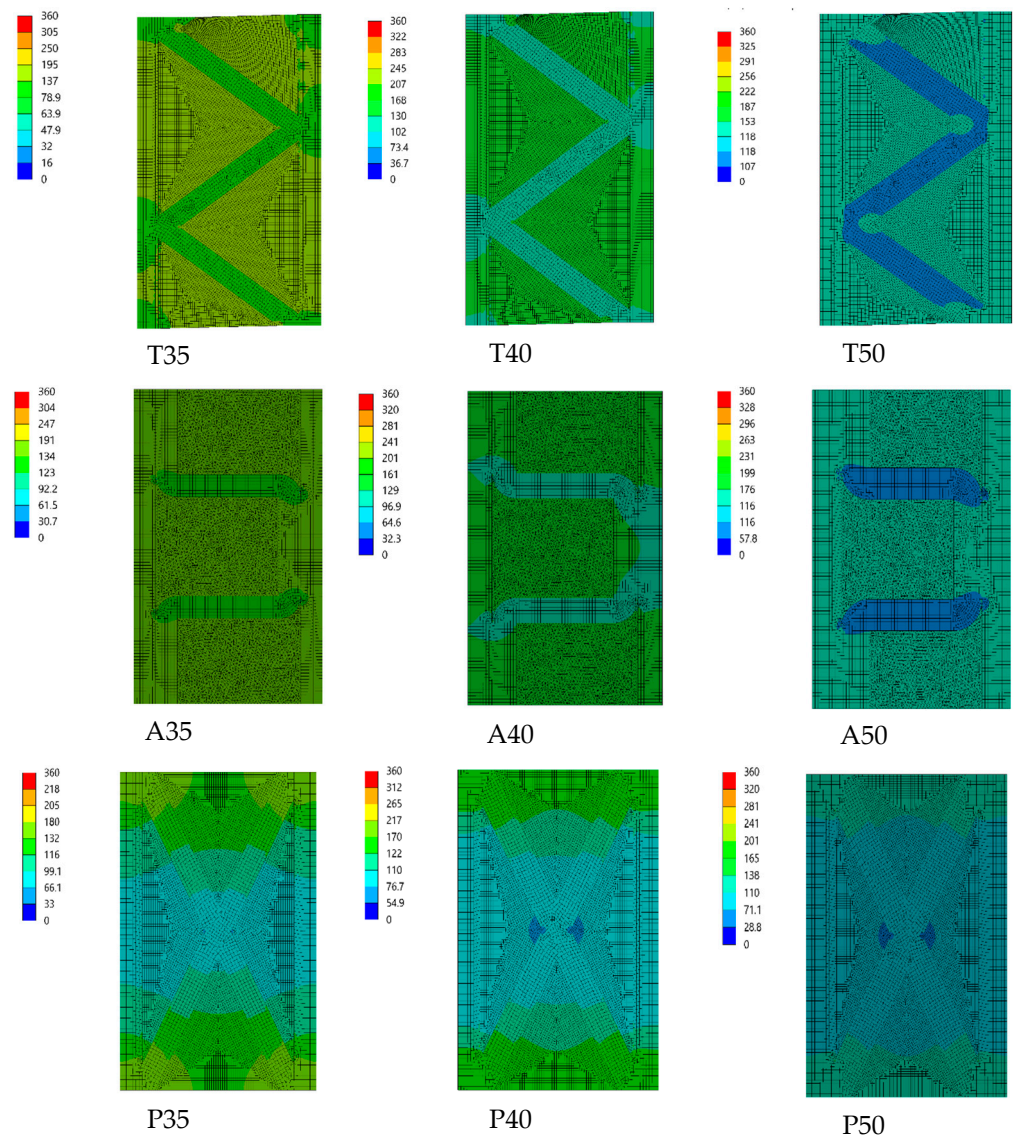


Figure 7. Surface heat flux contour maps with stagnant air in cavities.

On the other hand, the heat path through P walls is different from the first two types. Since P walls have two types of air layers, the thermal conductivities of these layers are different. In the larger voids, the heat transfer mechanism is the same as that of T and A walls. However, smaller voids have lower thermal conduction than the 3DPC. They have an insulative effect, and heat transfer occurs predominantly via the webs in these regions. Due to the presence of insulative air layers in P walls and their low void area, these walls exhibit the best thermal behavior. P35 has a U-value of $2.77 \text{ W/m}^2\cdot\text{K}$, while P50 has $1.947 \text{ W/m}^2\cdot\text{K}$. Therefore, the thermal performance of 3DPC lattice envelopes under stagnant air conditions in voids is mainly affected by the void area. T walls with the largest void area have the worst performance, while P walls with a smaller void area have the best thermal resistance. Figure 8 shows the thermal performance of the 3DPC envelopes with respect to their void area.

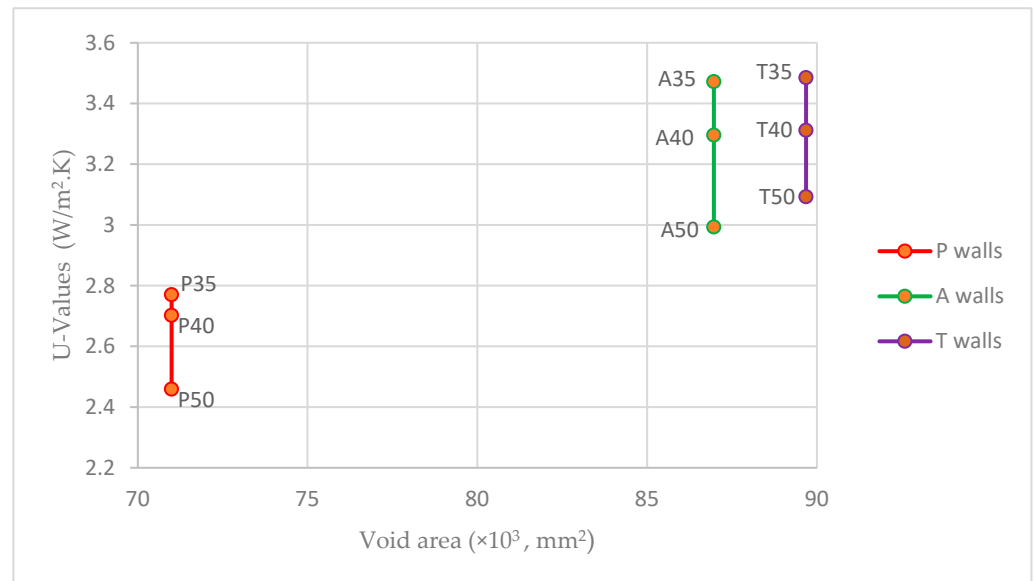


Figure 8. Thermal transmittance variations with void area.

3.2. Effect of Cavity Insulation

To improve the thermal inertia, EPS beads and loose fill perlite were applied in the cavities of the 3DPC lattice structures. The introduction of granular insulating materials significantly lowers the U-values for all wall types (Table 3). The thermal conductivity of the 3DPC is 32.6 and 21.8 times higher than that of EPS beads and loose-fill perlite, respectively (Table 1). Due to the high thermal conductivities between the 3DPC and the insulating materials, the heat path through all the insulated wall types is predominantly through the concrete webbing of the lattice structures. Thermal bridging is evident between the external and interior surfaces (Figures 9 and 10). Thermal bridges occur when highly conductive structural components penetrate the insulation plane [51].

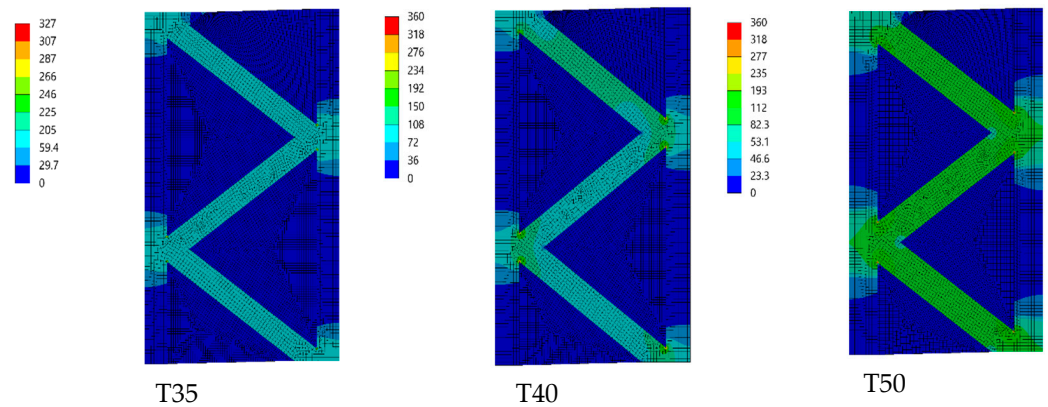


Figure 9. Cont.

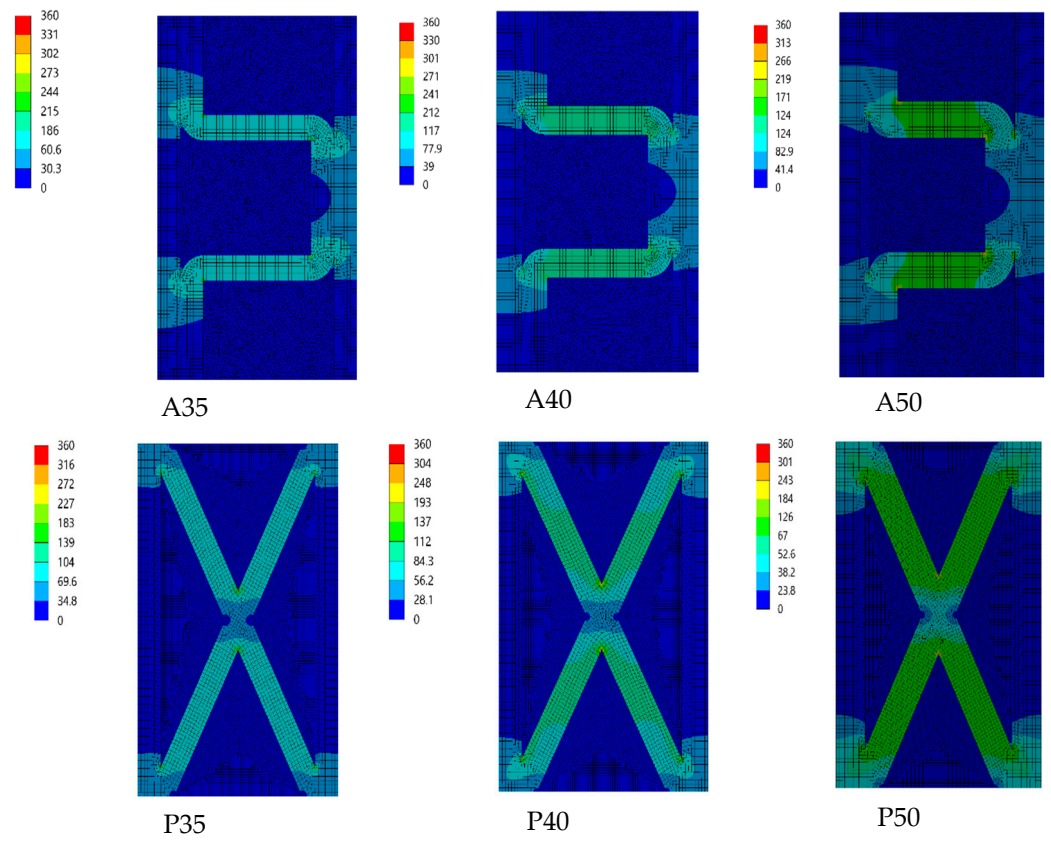


Figure 9. Surface heat flux contour maps of loose fill perlite insulated walls.

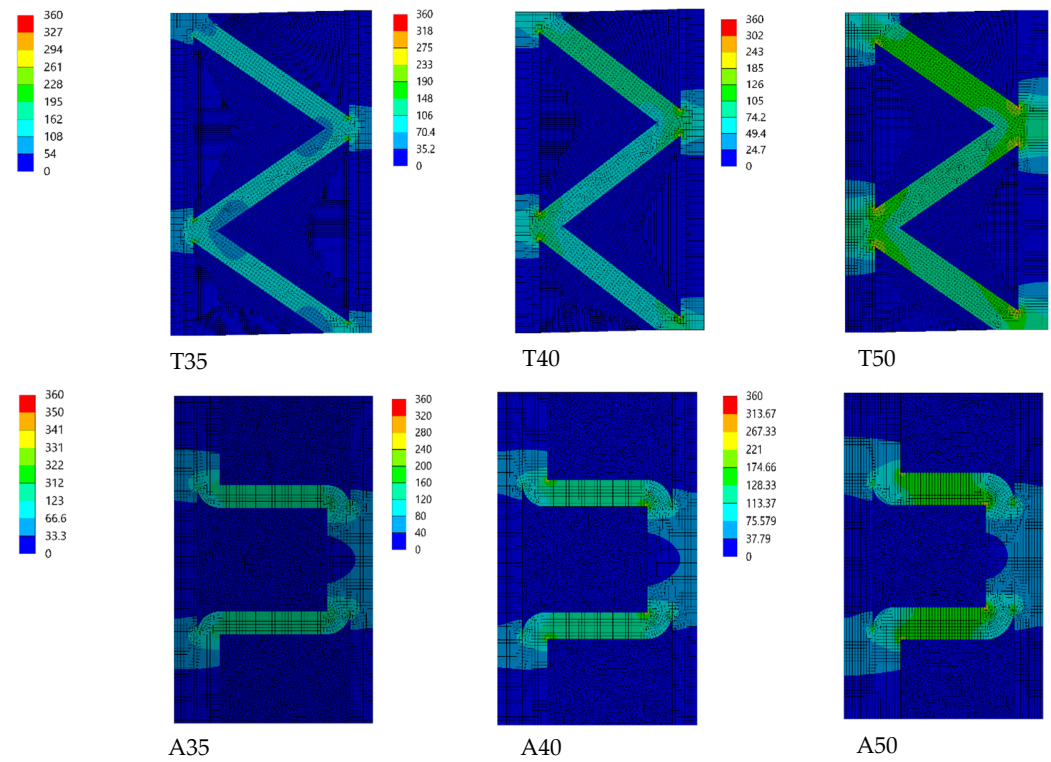


Figure 10. Cont.

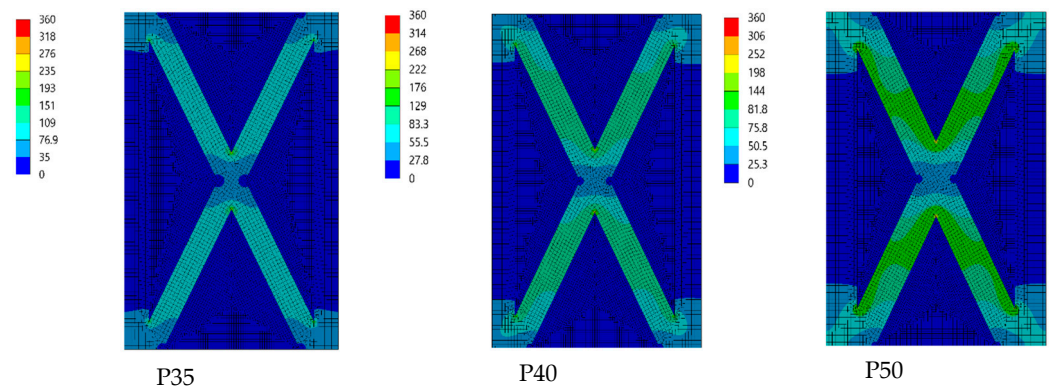


Figure 10. Surface heat flux contour maps of EPS insulated walls.

The percentage reductions in U-values in all wall types for both insulating materials are close and vary between 77.3 and 87.2% (Figure 11). Even though the percentage reductions due to EPS are slightly higher than those of perlite, the average difference is very small, i.e., 2.16% (Table 3). For example, for the 35 mm filament width with EPS insulation, the percentage reductions in U-values for T35, A35, and P35 are 87.23%, 86.95%, and 84.95%, respectively. This shows that cavity insulation significantly improves the thermal performance of 3DPC envelopes, which complements the results presented by Alkhalidi and Hatuqay [9]. Overall, P-walls show the best thermal performance of all wall types. For example, P50 has $0.154 \text{ W/m}^2\cdot\text{K}$ has the lowest U-value, and A50 has $0.563 \text{ W/m}^2\cdot\text{K}$ has the highest U-value of all EPS-insulated walls. This thermal behavior is contrary to the respective areas of insulation of the wall types. While cavity insulation significantly improves the thermal performance of 3DPC envelopes, there is a contradiction with the results presented by Suntharalingam et al. [15]. Their results showed that U-values decreased with an increase in void area with insulation due to larger amounts of insulation directing a reduction in material conductivities. However, the results of the current study say otherwise. T walls have the largest area of insulation of the three wall types in this study, while those of P walls are the smallest. Yet P-walls show the best thermal performance of all wall types. From the U-values of insulated lattice structures of the same thickness, contour lengths, and insulation percentage, it can be deduced that the individual differences in the thermal performance of 3DPC structures are not affected by the area of insulation but rather by thermal bridging resulting from the geometric properties of the structures. Figure 12 shows the thermal performance of the 3DPC envelopes with respect to their area of insulation.

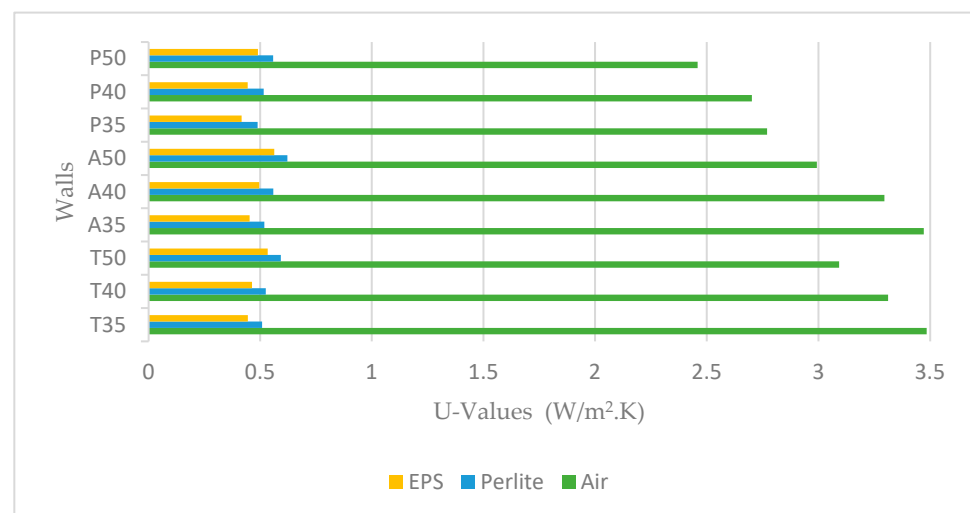


Figure 11. Reductions in U-values due to cavity insulation.

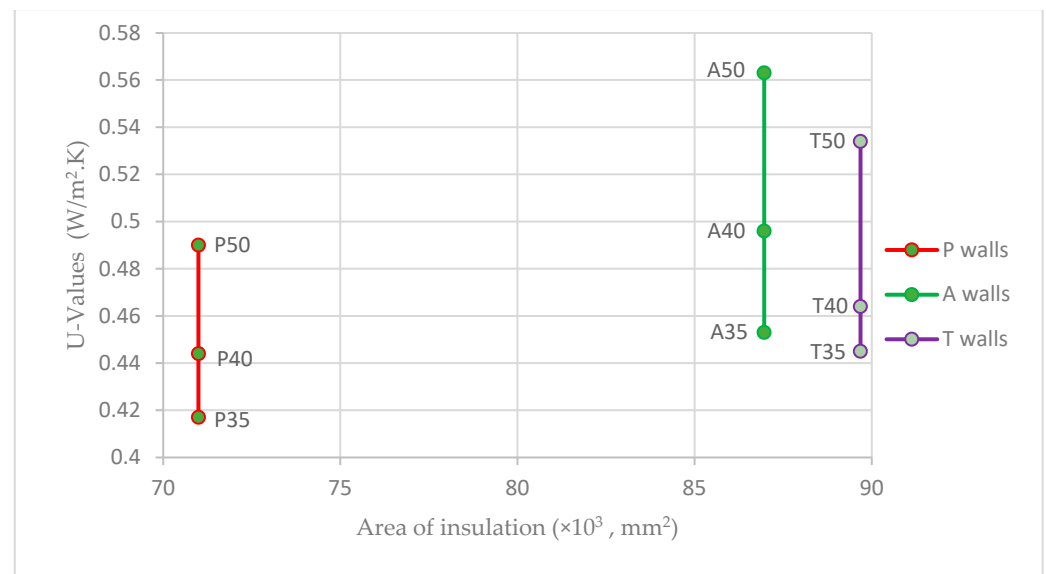


Figure 12. Thermal transmittance variations with area of insulation.

3.3. Effect of Geometric Properties of Insulated Lattice Structures

Of the three wall types, the P walls have the longest webs due to their cob design. The webs in these walls cross each other at a small slant angle compared to those of the T walls, with webs subtending a larger angle of inclination (Figure 6). This makes the P walls have the longest web length (heat path), followed by the T walls. The webs of the A walls are the shortest since they are perpendicular to the exterior and interior surfaces of the lattice structures. It means that there is a short and more direct bridge between the two wall faces. For instance, for the 35 mm filament width, the web lengths for the P35, T35, and A35 are 479, 288, and 245 mm, respectively. Since heat transfer through these insulated lattice structures is predominantly by conduction through the webs, heat takes the longest distance to travel through the P walls and the shortest distance from the A walls. This partly explains why the P walls have the lowest U-values and the A walls the highest. Similar observations were made by Pierzchlewicz [52], who compared the thermal performance of multicore and solid blocks. The researcher found that, when compared to multicore blocks with aligned holes, those with staggered holes elongate the heat flow path through walls. This improves the thermal resistance of the multicore blocks with staggered holes.

Furthermore, the contact or intersection area between the webs and face shells might also contribute to the thermal behavior of these insulated lattice envelopes. The A walls have the largest contact area of the three wall types. For instance, for the 35 mm filament width, the contact distance of A35 is 158 mm, whereas that of T35 and P35 is 36 mm and 37 mm, respectively. A large contact or intersection area means heat flow happens over a larger area. Similar observations were made by NCMA [53], who studied heat transfer through concrete blocks with different numbers of webs. They found a 30% reduction in the thermal resistance of concrete blocks with two webs over the typical three-web concrete blocks.

Lastly, across all walls of the same type, the U-value increases with an increase in the filament width. For example, the U-values of the perlite-insulated T walls, T35, T40, and T50 are 0.509, 0.525, and 0.593 W/m².K. This is because an increase in filament width implies an increase in the cross-sectional area of the webs. Since thermal bridging is predominant, the area through which heat travels increases, thereby reducing the thermal performance. The thermal performance of insulated 3DPC envelopes of the same contour lengths and percentage of insulation is mainly affected by the web length, filament width, and the contact (intersection) area between the webs and face shells.

3.4. Thermal Efficiency of Insulation

The thermal efficiency (T_{Eff}) of the insulation was calculated to determine its effectiveness. Thermal bridges significantly affect the effectiveness of the insulation, as discussed in the previous sections. This is because of the large thermal conductivity differences between the 3DPC and the granular fill materials. The thermal efficiency of both insulating materials in all wall types varies between 26 and 44% (Table 4 and Figure 13). This shows that 56–74% of the applied insulation is not used and does not contribute to increasing the thermal resistance of the lattice structures. Therefore, to reduce the effect of thermal bridges that undermine the effective use of insulation, innovative wall designs such as combined double-row walls, which minimize or eliminate web connections, are a potential solution. Other insulation techniques, such as internal wall insulation and the use of 3D printed lightweight concretes, are other potential solutions. Higher-density concrete tends to have more compressive strength than lightweight concrete, but lightweight concrete has a lower thermal conductivity [50]. The smaller the difference in thermal conductivities between the 3DPC and insulation fill material, the lower the effects of thermal bridging. This explains why perlite-insulated walls have slightly higher thermal efficiencies of insulation than EPS-insulated walls.

Table 4. Thermal efficiency of insulation of perlite and EPS.

Wall Configuration	R_{un}	R_{in} (K·m/W)		R_{eq} (K·m/W)		T_{Eff} (%)	
		Perlite	EPS	Perlite	EPS	Perlite	EPS
T35	0.287	1.965	2.247	4.234	5.650	39.63	34.70
T40	0.302	1.905	2.155	4.167	5.556	38.47	33.36
T50	0.323	1.686	1.873	3.922	5.236	34.76	29.59
A35	0.288	1.927	2.208	4.132	5.525	39.66	34.74
A40	0.303	1.789	2.016	4.098	5.464	36.25	31.34
A50	0.334	1.608	1.776	4.000	5.348	31.84	26.97
P35	0.361	2.045	2.398	3.861	5.155	43.62	39.52
P40	0.370	1.938	2.252	3.774	5.025	41.55	37.45
P50	0.407	1.792	2.041	3.597	4.808	38.52	33.99

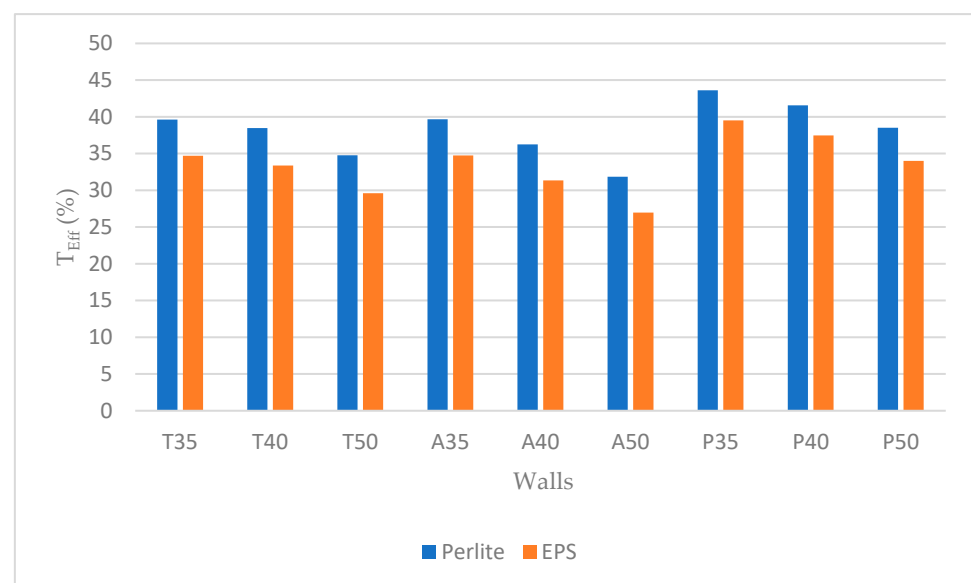


Figure 13. Thermal Efficiency (T_{Eff}) of Insulation of Perlite and EPS.

When it comes to 3D-printed concrete, the generally traditional materials adopted are mainly cement and fine sand in most cases. It is worth noting that, despite the study focusing on 3DPC made of traditional materials, researchers have developed and applied

various innovative materials. These range from different supplement cementitious materials (SCMs), phase change materials (PCM), admixtures, fibers, and different aggregate types [54,55]. When applied, all these materials have the potential to affect thermal performance based on their quantities and thermal conductivities.

By volume, aggregates, which occupy 60–70% of the volume of concrete, play an important role in the thermal performance of concrete [55]. Lightweight aggregates are typically associated with low densities and low thermal conductivities. This is the case for recycled sand, which has growing applications in construction due to sustainability concerns. Mohammad et al. [56] developed a high-performance lightweight concrete for 3D printing, while Pietras et al. [57] developed a novel 3D printing cement-based composite material with granulated cork. The application of such materials improves the thermal performance of 3DPC envelopes.

Coarse aggregate application in 3DPC, however, is an unavoidable development for a variety of 3DPC applications in construction. Ji et al. [58] introduced large-scale applications of coarse aggregates in 3DPC. Coarse aggregates have higher densities and thermal conductivities, thereby comprising thermal performance. SCMs, PCM, admixtures and fibers also have the potential to influence the thermal properties of 3DPC. When compared to ordinary concrete, 3DPC tends to have a higher percentage of entrained air bubbles. This is due to the use of viscosity-modifying and enhancing admixtures to maintain the desired rheological properties. Furthermore, additional air is entrapped between 3DPC layers during the printing process because of the nature of layer-to-layer construction. Both entrained and entrapped air volumes may have the potential to enhance the thermal resistivity of 3DPC. Hao et al. [59] studied the thermal conductivity of 3DPC made of recycled fine aggregate and PCM. Under the same size, density class, or mix design, they noted that the thermal conductivity of the 3DPC can reach up to 31.04% lower than that of mold-cast concrete. The replacement ratios of cement with SCMs by volume fraction are relatively small, and in the case of fibers, with a typical volume fraction of 2%, their application could almost be insignificant [60]. Other innovative materials that have found application in 3DPC are copper tailings, paraffin, and geopolymers, which have the potential to influence the thermal properties [61,62]. The composition of the mix designs of 3DPC presents opportunities for research into their effects on the thermal performance of 3DPC.

4. Conclusions

This work is a numerical study of 3DPC lattice envelopes to understand the influence of the geometry of the infill structure on their thermal performance. With emphasis on the buildability, scalability, and application of 3D concrete printing, the study was limited to lattice structures produced by the Material Deposition Method (extrusion). A holistic selection approach was taken in the selection of the three infill structures used in this study. This is to ensure that the lattice structures studied not only have sufficient structural integrity but are also consistent with additive manufacturing industrial trends. All the lattice structures were modeled to have nearly equal contour lengths and void and insulation percentages. Additionally, the effects of filament width and the application of granular insulating material (EPS beads and loose-fill perlite) were also studied. Lastly, the efficacy of insulation was also established to determine the extent to which unintended thermal bridges produce significant heat losses, resulting in the ineffective usage of the insulation material. Based on the findings of the analysis, the following conclusions were reached:

1. The thermal performance of 3DPC envelopes in stagnant air conditions is primarily influenced by the void area. T walls with the largest void area have the worst performance.
2. When the cavities are insulated, the individual differences in the thermal performance of 3DPC structures are not influenced by insulation area but by thermal bridging due to geometric properties. Despite having the smallest insulation area, P-walls show the best thermal performance among all wall types.

3. The thermal performance of insulated 3DPC envelopes of the same contour lengths is mainly affected by the web length, filament width, and the contact (intersection) area between the webs and face shells.
4. Due to varying web lengths, heat travels the longest distance through the P walls and the shortest distance from the A walls via thermal bridging. Furthermore, a large contact or intersection area between the webs and face shells, as in the case of the A walls, reduces thermal performance.
5. The U-values of insulated lattice structures increase with an increase in the filament width. This is because of the increase in the cross-sectional area of the webs, through which thermal bridging is predominant.
6. The application of EPS beads shows better thermal performance than that of loose fill perlite, owing to the lower thermal conductivity of EPS beads. To reduce thermal bridges and improve the effective use of insulation, the use of innovative wall designs, together with other insulation techniques and lightweight concrete, is recommended.

These results provide designers with insights to consider when planning buildings' energy needs. This study broadens our understanding and gives a better insight into the energy performance of building systems and cost-effective options during the adoption of additive manufacturing in the construction industry.

Author Contributions: Software, validation, investigation, data curation, writing—original draft preparation, visualization: K.C. Conceptualization, methodology, formal analysis, writing—review and editing, supervision: Ç.Y. All authors have read and agreed to the published version of the manuscript.

Funding: This research received no external funding.

Data Availability Statement: The data presented in this study are available on request from the corresponding author.

Acknowledgments: This paper is produced from the first author's Master of Science thesis under the supervision of the second author. The first author thanks the government of Türkiye for the Türkiye Scholarships (Türkiye Bursları).

Conflicts of Interest: The authors declare no conflicts of interest.

References

1. Di Foggia, G. Energy efficiency measures in buildings for achieving sustainable development goals. *Energy Procedia* **2018**, *134*, 702–711. [[CrossRef](#)] [[PubMed](#)]
2. Sakin, M.; Kiroglu, Y.C. 3D Printing of Buildings: Construction of the Sustainable Houses of the Future by BIM. *Energy Procedia* **2017**, *134*, 702–711. [[CrossRef](#)]
3. Apis Cor. Construction with Robotic Precision. Technologies. Available online: <https://apis-cor.com/technologies/> (accessed on 21 December 2023).
4. Zhao, Z.; Ji, C.; Xiao, J.; Yao, L.; Lin, C.; Ding, T.; Ye, T. A critical review on reducing the environmental impact of 3D printing concrete: Material preparation, construction process and structure level. *Constr. Build. Mater.* **2023**, *409*, 133887. [[CrossRef](#)]
5. Heng, G.; Ting, A.; Wei, Y.; Tay, D.; Qian, Y.; Tan, M.J. Utilization of recycled glass for 3D concrete printing: Rheological and mechanical properties. *J. Mater. Cycles Waste Manag.* **2019**, *21*, 994–1003. [[CrossRef](#)]
6. Voskresenskaya, E.; Vorona-Slivinskaya, L.; Panov, S. Legal regulation of environmental protection, management of natural resources, and environmental safety in construction sector. *MATEC Web Conf.* **2018**, *193*, 02025. [[CrossRef](#)]
7. Jipa, A.; Dillenburger, B. 3D Printed Formwork for Concrete: State-of-the-Art, Opportunities, Challenges, and Applications. *3D Print. Addit. Manuf.* **2022**, *9*, 84–107. [[CrossRef](#)] [[PubMed](#)]
8. Berman, B.; Zarb, F.G. 3-D printing: The new industrial revolution. *Bus. Horiz.* **2012**, *55*, 155–162. [[CrossRef](#)]
9. Alkhalidi, A.; Hatuqay, D. Energy efficient 3D printed buildings: Material and techniques selection worldwide study. *J. Build. Eng.* **2020**, *30*, 101286. [[CrossRef](#)]
10. Mechtcherine, V.; Nerella, V.N.; Will, F.; Näther, M.; Otto, J.; Krause, M. Large-scale digital concrete construction-CONPrint3D concept for on-site, monolithic 3D-printing. *Autom. Constr.* **2019**, *107*, 102933. [[CrossRef](#)]
11. Apis Cor. Progress on 3D Printing. Available online: https://www.linkedin.com/posts/apis-cor_3dprinted-wall-concrete-activity-7142975182201110528-FrU?utm_source=share&utm_medium=member_android (accessed on 22 December 2023).

12. Hens, H. Ambient conditions, building performance and material properties. In *Applied Building Physics*; John Wiley & Sons.: Hoboken, NJ, USA, 2016. Available online: https://books.google.com/books/about/Applied_Building_Physics.html?id=fdo7CwAAQBAJ (accessed on 24 January 2024).
13. Mansouri, A.; Binali, A.; Aljawi, A.; Alhammadi, A.; Almir, K.; Alnuaimi, E.; Alyousuf, H.; Rodriguez-Ubinas, E. Thermal modeling of the convective heat transfer in the large air cavities of the 3D concrete printed walls. *Cogent. Eng.* **2022**, *9*, 2130203. [[CrossRef](#)]
14. Nemova, D.; Kotov, E.; Andreeva, D.; Khorobrov, S.; Olshevskiy, V.; Vasileva, I.; Zaborova, D.; Musorina, T. Experimental Study on the Thermal Performance of 3D-Printed Enclosing Structures. *Energies* **2022**, *15*, 4230. [[CrossRef](#)]
15. Suntharalingam, T.; Upasiri, I.; Gatheeshgar, P.; Poologanathan, K.; Nagaratnam, B.; Santos, P.; Rajanayagam, H. Energy Performance of 3D-Printed Concrete Walls: A Numerical Study. *Buildings* **2021**, *11*, 432. [[CrossRef](#)]
16. Faruk, O.; Bledzki, A.K.; Fink, H.-P.; Sain, M. Biocomposites reinforced with natural fibers: 2000–2010. *Prog. Polym. Sci.* **2012**, *37*, 1552–1596. [[CrossRef](#)]
17. Stark, N.M.; Matuana, L.M. Characterization of weathered woodeplastic composite surfaces using FTIR spectroscopy, contact angle, and XPS. *Polym. Degrad. Stab.* **2007**, *92*, 1883–1890. [[CrossRef](#)]
18. Parker, K.; Garancher, J.P.; Shah, S.; Fernyhough, A. Expanded polylactic acid—An eco-friendly alternative to polystyrene foam. *J. Cell. Plast.* **2011**, *47*, 233–243. [[CrossRef](#)]
19. AlZahrani, A.A.; Alghamdi, A.A.; Basalah, A.A. Computational Optimization of 3D-Printed Concrete Walls for Improved Building Thermal Performance. *Buildings* **2022**, *12*, 2267. [[CrossRef](#)]
20. Ochs, F.; Müller-Steinhagen, H. Temperature and Moisture Dependence of the Thermal Conductivity of Insulation Materials. 2005. Available online: www.itw.uni-stuttgart.de (accessed on 24 January 2024).
21. Abidi, S.; Nait-Ali, B.; Joliff, Y.; Favotto, C. Impact of perlite, vermiculite and cement on the thermal conductivity of a plaster composite material: Experimental and numerical approaches. *Compos. Part B Eng.* **2014**, *68*, 392–400. [[CrossRef](#)]
22. QOROX, “Leading Printed Structures Welcoming Freeform Design Opportunities”. 2023. Available online: <https://qorox.co.nz/wp-content/uploads/2022/09/QOROX-Brochure-V7.pdf> (accessed on 20 December 2023).
23. Santos, G.H.D.; Fogiatto, M.A.; Mendes, N. Numerical analysis of thermal transmittance of hollow concrete blocks. *J. Build. Phys.* **2017**, *41*, 7–24. [[CrossRef](#)]
24. Pessoa, S.; Jesus, M.; Guimarães, A.S.; Lucas, S.S.; Simões, N. Experimental characterisation of hygrothermal properties of a 3D printed cementitious mortar. *Case Stud. Constr. Mater.* **2023**, *19*, e02355. [[CrossRef](#)]
25. Schiavoni, S.; D’alessandro, F.; Bianchi, F.; Asdrubali, F. Insulation materials for the building sector: A review and comparative analysis. *Renew. Sustain. Energy Rev.* **2016**, *62*, 988–1011. [[CrossRef](#)]
26. Al Tamimi, A.; Hassan, H.; Rodriguez-Ubinas, E.; Alhaidary, H.; Mansouri, A. Thermal performance of 3D concrete printed walls: Calculated and in-situ measured U-values. *J. Asian Archit. Build. Eng.* **2023**. [[CrossRef](#)]
27. Ouedraogo, E.; Ouédraogo, E.; Coulibaly, O.; Kaboré, B.; Imbga, K.B.; Ouédraogo, A. Optimization of the air gap thickness for the insulation of double-walled walls of a building. *Asian J. Sci. Technol.* **2018**, *9*, 8786–8794. Available online: <https://www.researchgate.net/publication/328743687> (accessed on 24 January 2024).
28. ISO 6946: 2017; Building Components and Building Elements—Thermal Resistance and Thermal Transmittance—Calculation Methods. International Organisation of Standardization (ISO): Geneva, Switzerland, 2017. Available online: <https://www.iso.org/standard/65708.html> (accessed on 24 January 2024).
29. Simpson, A.; Stuckest, A.D. Thermal conductivity of porous materials: II Theoretical treatment of radiative heat transfer. *Build. Serv. Eng. Res. Technol.* **1990**, *11*, 13–19. [[CrossRef](#)]
30. Ju, J.; Schellenberg, J.; Wallis, M. Dependence of Thermal Properties of Expandable Polystyrene Particle Foam on Cell Size and Density. *J. Cell. Plast.* **2010**, *46*, 209–222. [[CrossRef](#)]
31. Simpson, A.; Rattigan, I.G.; Kalavsky, E.; Parr, G. Thermal conductivity and conditioning of grey expanded polystyrene foams. *Cell. Polym.* **2020**, *39*, 238–262. [[CrossRef](#)]
32. Ismaiel, M.; Chen, Y.; Cruz-Noguez, C.; Hagel, M. Thermal resistance of masonry walls: A literature review on influence factors, evaluation, and improvement. *J. Build. Phys.* **2022**, *45*, 528–567. [[CrossRef](#)]
33. Ono, R. Parâmetros para garantia da qualidade do projeto de segurança contra incêndio em edifícios altos. *Ambiente Construído* **2008**, *7*, 97–113. Available online: <https://seer.ufrgs.br/index.php/ambienteconstruido/article/view/3731> (accessed on 24 January 2024).
34. Rigão, A.O. Comportamento de Pequenas Paredes de Alvenaria Estrutural Frente a Altas Temperaturas. August 2012. Available online: <http://repositorio.ufsm.br/handle/1/7809> (accessed on 24 January 2024).
35. Famà, A.; Restuccia, L.; Ván, P. Generalized ballistic-conductive heat transport laws in three-dimensional isotropic materials. *Contin. Mech. Thermodyn.* **2021**, *33*, 403–430. [[CrossRef](#)]
36. Sun, J.; Xiao, J.; Li, Z.; Feng, X. Experimental study on the thermal performance of a 3D printed concrete prototype building. *Energy Build.* **2021**, *241*, 110965. [[CrossRef](#)]
37. Lu, G.; Liu, Y.; Kang, J.; Lyu, M.; Lai, Y.; Dong, Z. Numerical modeling and experimental verification for anisotropic heat conduction process in velocity probe of the thermal mass flowmeter. *Appl. Therm. Eng.* **2024**, *236*, 1359–4311. [[CrossRef](#)]
38. Daungwilailuk, T.; Pheinsusom, P.; Pansuk, W. Uniaxial load testing of large-scale 3D-printed concrete wall and finite-element model analysis. *Constr. Build. Mater.* **2021**, *275*, 122039. [[CrossRef](#)]

39. Joh, C.; Lee, J.; Bui, T.Q.; Park, J.; Yang, I.H. Buildability and Mechanical Properties of 3D Printed Concrete. *Materials* **2020**, *13*, 4919. [[CrossRef](#)] [[PubMed](#)]
40. Bello, N.D.; Memari, A.M. Comparative Review of the Technology and Case Studies of 3D Concrete Printing of Buildings by Several Companies. *Buildings* **2023**, *13*, 106. [[CrossRef](#)]
41. WASP. 3D Printer House | Crane WASP. Available online: <https://www.3dwasp.com/en/3d-printer-house-crane-wasp/> (accessed on 23 December 2023).
42. Alhumayani, H.; Gomaa, M.; Soebarto, V.; Jabi, W. Environmental assessment of large-scale 3D printing in construction: A comparative study between cob and concrete. *J. Clean. Prod.* **2020**, *270*, 122463. [[CrossRef](#)]
43. Black Buffalo 3D. NEXCON Brochure. Available online: <https://bb3d.io/nexcon-brochure/> (accessed on 24 December 2023).
44. Schumacher, C.J.; Straube, J.F.; Ober, D.G.; Grin, A.P. Development of a new hot box apparatus to measure building enclosure thermal performance. In Proceedings of the Thermal Performance of the Exterior Envelopes of Whole Buildings XII International Conference—ASHRAE, Clearwater, FL, USA, 1–5 December 2013.
45. Insulation Company of America. What is Expanded Polystyrene (EPS) Foam? The Possibilities Are Endless! Available online: <https://insulationcorp.com/eps/> (accessed on 20 December 2023).
46. Yucel, K.T.; Basyigit, C.; Ozel, C. Thermal insulation properties of expanded polystyrene as construction AND insulating materials. *Constr. Build. Mater.* **2020**, *263*, 120674. Available online: <https://www.researchgate.net/publication/237669763> (accessed on 24 January 2024).
47. Davraz, M.; Koru, M.; Akdag, A.; Kılınçarslan, S.İ.; Delikanlı, Y.; Çabuk, M. Investigating the use of raw perlite to produce monolithic thermal insulation material. *Constr. Build. Mater.* **2020**, *263*, 120674. [[CrossRef](#)]
48. Perlite Institute. Perlite and the Environment. Available online: <https://www.perlite.org/environmental/> (accessed on 24 December 2023).
49. Jan Kosny, P.; Yarbrough, P.D.; Childs, P.; Mohiuddin, P.S.A. How the Same Wall Can Have Several Different R-Values: Relations Between Amount of Framing and Overall Thermal Performance in Wood and Steel-Framed Walls. In Proceedings of the ASHRAE THERM X, Thermal Performance of the Exterior Envelopes of Buildings X, Clearwater, FL, USA, 2–5 December 2007.
50. Urban, B.; Engelmann, P.; Kossecka, E.; Kosny, J. Arranging Insulation for Better Thermal Resistance in Concrete and Masonry Wall Systems. In Proceedings of the 9th Nordic Symposium on Building Physics, Tampere, Finland, 29 May–2 June 2011; Volume 29. Available online: <https://www.researchgate.net/publication/266602609> (accessed on 24 January 2024).
51. Canadian Concrete Masonry Producers Association (CCMP). *Metric Technical Manual—Thermal Properties & Design Details (Section 6)*; CCMP: Toronto, ON, Canada, 2013. Available online: <https://ccmpa.ca/download/metric-technical-manual/> (accessed on 16 December 2023).
52. Pierzchlewicz, J. Modern Concrete Wall-Units with Improved Thermal Resistance for Housing in Hot Climate. *Sultan Qaboos Univ. J. Sci. [SQUJS]* **1996**, *1*, 69–80. [[CrossRef](#)]
53. National Concrete Masonry Association (NCMA). Thermal Catalog of Concrete Masonry Assemblies. Available online: <https://ncma.org/resource/thermal-catalog-of-concrete-masonry-assemblies/> (accessed on 18 December 2023).
54. Zhang, C.; Nerella, V.N.; Krishna, A.; Wang, S.; Zhang, Y.; Mechtcherine, V.; Banthia, N. Mix design concepts for 3D printable concrete: A review. *Cem. Concr. Compos.* **2021**, *122*, 104155. [[CrossRef](#)]
55. Hou, S.; Duan, Z.; Xiao, J.; Ye, J. A review of 3D printed concrete: Performance requirements, testing measurements and mix design. *Constr. Build. Mater.* **2020**, *273*, 121745. [[CrossRef](#)]
56. Mohammad, M.; Masad, E.; Seers, T.; Al-Ghamdi, S.G. High-Performance Light-Weight Concrete for 3D Printing. *RILEM Bookseries* **2020**, *28*, 459–467. [[CrossRef](#)]
57. Pietras, D.; Zbyszynski, W.; Sadowski, T. A 3D Printing Method of Cement-Based FGM Composites Containing Granulated Cork, Polypropylene Fibres, and a Polyethylene Net Interlayer. *Materials* **2023**, *16*, 4235. [[CrossRef](#)] [[PubMed](#)]
58. Ji, G.; Ding, T.; Xiao, J.; Du, S.; Li, J.; Duan, Z. A 3D Printed Ready-Mixed Concrete Power Distribution Substation: Materials and Construction Technology. *Materials* **2019**, *12*, 1540. [[CrossRef](#)] [[PubMed](#)]
59. Hao, L.; Xiao, J.; Sun, J.; Xia, B.; Cao, W. Thermal conductivity of 3D printed concrete with recycled fine aggregate composite phase change materials. *J. Clean. Prod.* **2022**, *364*, 132598. [[CrossRef](#)]
60. Soltan, D.G.; Li, V.C. A self-reinforced cementitious composite for building-scale 3D printing. *Cem. Concr. Compos.* **2018**, *90*, 1–13. [[CrossRef](#)]
61. Al-Qutaifi, S.; Nazari, A.; Bagheri, A. Mechanical properties of layered geopolymer structures applicable in concrete 3D-printing. *Constr. Build. Mater.* **2018**, *176*, 690–699. [[CrossRef](#)]
62. Ma, G.; Li, Z.; Wang, L. Printable properties of cementitious material containing copper tailings for extrusion based 3D printing. *Build. Mater.* **2018**, *162*, 613–627. [[CrossRef](#)]

Disclaimer/Publisher’s Note: The statements, opinions and data contained in all publications are solely those of the individual author(s) and contributor(s) and not of MDPI and/or the editor(s). MDPI and/or the editor(s) disclaim responsibility for any injury to people or property resulting from any ideas, methods, instructions or products referred to in the content.